

How large is the population of heavily obscured X-ray sources?

Filippo Frontera^{1,2}, Mauro Orlandini¹, Raffaella Landi¹, Andrea Comastri³, Fabrizio Fiore⁴, Giancarlo Setti^{5,6}, Lorenzo Amati¹, Enrico Costa⁷, Nicola Masetti¹, and Eliana Palazzi¹

¹*INAF/Istituto di Astrofisica Spaziale e Fisica Cosmica, Bologna, Via Gobetti 101, 40129 Bologna, Italy*

²*Dipartimento di Fisica, Università di Ferrara, Via Saragat, 1, 44100 Ferrara, Italy*

³*INAF/Osservatorio Astronomico di Bologna, Via Ranzani, 1, 40127 Bologna, Italy*

⁴*INAF/Osservatorio Astronomico di Roma, 00040 Monte Porzio Catone, Italy*

⁵*Dipartimento di Astronomia, Università di Bologna, Via Ranzani, 1, 40127 Bologna, Italy*

⁶*INAF/Istituto di Radioastronomia di Bologna, Via Gobetti, 101, 40129 Bologna, Italy*

⁷*INAF/Istituto di Astrofisica Spaziale e Fisica Cosmica, Roma, Via del Fosso del Cavaliere 100, 00133 Roma, Italy*

The precise origin of the Cosmic X-ray Background (CXB) is still a matter of debate, although it is widely believed that the main contribution comes from active galactic nuclei (AGNs), powered by accreting supermassive black holes (BHs) ¹⁻³. At high energies (> 10 keV), where most of the flux resides and only a small fraction has been resolved into sources, obscured AGNs are the most likely contributors. While the CXB spectral shape (> 3 keV) appears to be well determined, its intensity is still uncertain: in the 2–10 keV interval the results disagree by a factor up to 1.5 (Refs. 4, 5), while at energies > 15 keV the normalization of the best available measurement ⁶ is questioned ⁷⁻¹³. Here we report on an accurate measurement of the CXB in the 15–50 keV range, establishing a most likely intensity level at 30 keV of $40 \text{ keV cm}^{-2} \text{ s}^{-1} \text{ sr}^{-1}$, while a normalization 12% higher than that of the best available past measurements ⁶ is marginally consistent with our data. In combination with the CXB synthesis models we infer that about 25% of the intensity at 30 keV arises from extremely obscured, Compton thick AGNs (absorbing column density $N_{\text{H}} > 10^{24} \text{ cm}^{-2}$), while a much larger population would be implied by the highest intensity estimates ³. We also infer a mass density of supermassive BHs of $3 \cdot 10^5 \text{ M} \cdot \text{Mpc}^{-3}$. The summed contribution of resolved sources ¹⁴ in the 2–10 keV band exceeds our best fit CXB intensity, but it is within our upper limit, so that any significant contribution to the CXB from sources other than AGNs, such as star forming galaxies and diffuse Warm-Hot Intergalactic Medium (WHIM), is expected to be mainly confined below a few keV.

After the first pioneer CXB measurements ¹⁵, the major effort to get a reliable estimate of the spectrum in a broad energy band (2–400 keV) was performed in the late 1970’s with the A2 and A4 instruments aboard the *High Energy Astronomical Observatory 1 (HEAO–1)*. The A2 results (3–45 keV) were first presented by Marshall et al. ¹⁶ (see Table 1), while the final results obtained with the A4 Low Energy Detector (LED, 13–180 keV) were reported by Gruber et al. ⁶, who also presented the conclusive results by both experiments.

According to *HEAO–1* ⁶, the CXB energy spectrum $J(E)$ from 3 to 60 keV is given, within a few percentage points, by a power-law with a high energy exponential cutoff (CUTOFFPL, see Table 1), while the corresponding $E J(E)$ spectrum shows a characteristic bell shape with a maximum intensity of 42.6 keV (cm² s sr)^{–1} at 29.3 keV.

After *HEAO–1*, at low energies (< 10 keV) many other CXB measurements were performed with both imaging and non imaging telescopes aboard satellite missions, while at high energies (> 15 keV) no other measurement has been published yet (see Table 1). From this Table, we can see that the low energy measurements show a spread of the 2–10 keV CXB integrated intensity up to 40%, with the lowest CXB estimates obtained with *HEAO–1* A2 ¹⁶ and the highest with the focusing telescopes aboard *BeppoSAX* ¹⁷, *XMM-Newton* ^{8,18} and *Chandra* ⁵. Driven by these discordant results, several authors ^{7–13}, in their evaluation of the fraction of the CXB that can be resolved into individual sources or in their CXB source synthesis models, assume the 1–60 keV CXB spectrum obtained with *HEAO–1* ⁶ to be corrected in its shape, but underestimated in its intensity due to systematic errors in the flux scale calibration and/or instrumental background subtraction. As a result, the *HEAO–1* CXB intensity is increased upward by a factor up to 1.4, either at low and at high energies.

In order to establish whether such CXB intensity renormalization is justified, and thus to constrain the size of a population of highly obscured AGNs and to infer the presence of other source populations and/or of a truly diffuse component (WHIM, see Ref. 19), we have performed an accurate measurement of the total (resolved plus unresolved) high energy (> 15 keV) CXB intensity by exploiting the pointed observations performed with the *Phoswich Detection System (PDS)* aboard the *BeppoSAX* satellite ²⁰.

Although the PDS was not designed to perform a measurement of the CXB (Field of View, FOV, of only 1.3 FWHM), *a posteriori* it was realized that such measurement would be possible given the very good performance of the instrument: high temporal stability, very low background

level $B_{15-300\text{ keV}} = 1.6 \cdot 10^4 \text{ counts (cm}^2 \text{ s keV)}^{-1}$, high flux sensitivity and good energy calibration. The 15–300 keV limiting sensitivity corresponds to about 1% of the background level with a marginal influence (0.3%) of systematic errors in the background subtraction, also thanks to the continuous monitoring of the background with two rocking collimators which alternated with a default dwell time of 96 s between the neutral position (ON–source) and two default symmetrical positions offset by 3.5° (OFF–source). The PDS response function was determined from pre-launch calibrations combined with Monte Carlo calculations and was tested with several repeated observations of the Crab Nebula, finding that its 15–50 keV spectrum derived with the PDS is consistent with most of the available measurements within 8% (details in Supplementary Information, thereafter SI).

The measurement of the unresolved CXB photon spectrum stands as one of the most difficult tasks in the observational X–ray astronomy. Among other things, it requires the knowledge, for each energy channel, of the instrument intrinsic background count rate ϵ_{in} to be subtracted from the total background B_B^{sky} measured during the observation of a blank sky field ($B_B^{sky} = C_{XB} + \epsilon_{in}$, where C_{XB} is the CXB count rate entering through the telescope FOV). Systematic errors in the C_{XB} estimate can intervene either in a biased selection of blank fields or in a wrong ϵ_{in} evaluation or in both. (For the methods adopted by *HEAO–I* to derive the CXB spectrum, see SI.)

Our measurement of the unresolved C_{XB} count rate is based on the *Sky-Earth Pointing* (SEP) method, in which we subtract from the background level B_B^{sky} measured from a blank sky field ($B_B^{sky} = C_{XB} + \epsilon_{in}^{sky}$) the count rate level measured when the telescope is pointing to the dark Earth ($B_B^{Earth} = A + \epsilon_{in}^{Earth}$, where A is the count rate due to the X–ray terrestrial albedo entering through the telescope FOV). The difference spectrum $D(E) = (C_{XB} - A) + (\epsilon_{in}^{sky} - \epsilon_{in}^{Earth})$ becomes $D(E) = C_{XB} - A$ if $\epsilon_{in}^{Earth} = \epsilon_{in}^{sky}$. Given that the radiation environment does not change looking to the dark Earth or to the sky, the latter condition is expected to be satisfied if both measurements are performed at the same cutoff magnetic rigidity and at the same time distance from the South Atlantic Geomagnetic Anomaly. Thus, The difference $D(E)$ was derived only for Observation Periods (OPs) of ~ 10 ks duration during which the corresponding B_B^{sky} and B_B^{Earth} were measured at similar mean values of the cutoff rigidity. In addition, given that the instrument mass distribution exposed to the sky (or Earth) and thus the intrinsic background can change with the collimator offset angle, we separately derived $D(E)$ for the ON, + OFF and – OFF collimator positions. For the Earth pointings, we selected only those with the PDS axis well below the Earth limb. This method does not require a variable instrument configuration but requires the measurement of the albedo spectrum, which is not negligible at energies > 15 keV.

The SEP strategy was also adopted for the CXB measurement performed with the *ASCA* GIS²¹ and *BeppoSAX* MECS¹⁷ imaging telescopes, and with the *Rossi-XTE* PCA collimated detector²².

In order to satisfy the blank sky field condition, in addition to discarding all those pointings within 15° from the Galactic plane, we adopted a series of selection criteria described in SI. From the entire set of 868 *BeppoSAX* Observation Periods (OPs) off the Galactic plane, the number of useful OP number becomes 275 (127 ON-source, 71 + OFF-source, and 77 OFF-source) with a total exposure time of 4031 ks. The dark Earth was observed for a total of 2056 ks.

The difference spectra $D_{\text{ON}}(E)$, $D_{+\text{OFF}}(E)$, and $D_{-\text{OFF}}(E)$, derived for each of the three collimator positions, are shown and discussed in SI. Since these spectra are consistent with each other within their statistical uncertainties (see SI), we used their sum $D(E)$ shown in Fig. 1. As can be seen, $D(E)$ is well determined up to 50 keV. For the model fitting, $D(E)$ was rebinned following the standard criteria of having a sufficient number of counts/channel and not oversampling the instrument energy resolution. Its spectral shape confirms that the CXB spectrum is modified by the albedo radiation of the dark Earth and shows that the CXB spectral slope is steeper than that of the albedo from the dark Earth (see details in SI). Thus we fit $D(E)$ with the difference of two model spectra, one to describe the unresolved CXB spectrum and the other to describe the albedo radiation spectrum. For the albedo model spectrum, we used a photo-electrically absorbed power-law (PL) (see SI), while, for the CXB spectrum, we used a CUTOFFPL model, that gives the best description of the *HEAO-1* data⁶ and likely gives the correct shape of CXB spectrum, and a PL model, which in the 15–50 keV band gives a satisfactory description of the CXB shape derived with *HEAO-1* (see Table 1).

The deconvolved intensity per unit solid angle of both the CXB ($I_{\text{CXB}}(E)$) and the terrestrial albedo ($I_{\text{A}}(E)$) requires, in addition to the knowledge of the instrument response function, that of the PDS solid angle. (Both are discussed in SI.) The instrument solid angle is $\Omega = 4.624 \times 10^{-4}$ sr. In Fig. 1 we show the best fitting curve to $D(E)$ and the corresponding residuals under the assumption of a PL as input model for the unresolved CXB.

Using the PDS pointings, we also performed an estimate of the contribution of resolved sources to the 15–50 keV CXB intensity (see SI). We found that their contribution increases the total (resolved plus unresolved) CXB intensity by 4.7%. Adding the contribution of brighter sources does not significantly change this figure.

The best fit parameters of the total CXB spectrum and albedo, and the 20–50 keV integrated CXB intensity for each of the used input models are reported in Table 2. We report the best fit photon spectrum of the terrestrial albedo in SI, while in Fig. 2 we show, for the CUTOFFPL model, the best fit energy spectrum $J(E)$ and the corresponding $E J(E)$ spectrum of the total CXB, along with their comparison with the past results.

From the Fig. 2 and from the Table reported in SI, it is apparent that our best fit 20–50 keV CXB intensity is in full agreement with that obtained with *HEAO-1 A2*¹⁶, and slightly lower (from 3 to 10%, depending on the input model) than that obtained by Gruber et al.⁶. We find a mean value of the CXB flux density of $\sim 40 \text{ keV (cm}^2 \text{ s sr)}^{-1}$ at 30 keV. We have also evaluated the upper limit to the CXB intensity that can be marginally accommodated by our data, by exploring the space of all the parameters involved in the fits (see details in SI). We find that, independently of the CXB model, in 90% of this multi-parameter space the 20–50 keV integrated intensity is lower than $6.8 \cdot 10^8 \text{ erg cm}^{-2} \text{ s}^{-1} \text{ sr}^{-1}$, which is 12% higher than that quoted by Gruber et al.⁶ and 21% higher than that quoted by Marshall et al.¹⁶.

Even this upper limit disagrees with the extrapolation to higher energies of the low energy ($< 10 \text{ keV}$) CXB estimates obtained with the focusing telescopes aboard *BeppoSAX*¹⁷, *XMM-Newton*^{8,18}, and *Chandra*⁵ but it is consistent with those obtained with *ASCA*, and *RXTE*²³. Thus, if we exclude a change in the CXB spectral shape derived with *HEAO-1*, our results raise the issue about the origin of the highest CXB intensities being quoted at lower energies. Differences in the flux scale calibration do not appear to be the origin of these discrepancies. One may think that part of the discrepant results could be due to the amount of sky solid angle surveyed, which is very large in the case of *HEAO-1* and *BeppoSAX* PDS and very small in the case of *BeppoSAX* MECS, *XMM-Newton* and *Chandra* (see last figure of SI), although, as also discussed by Barcons et al.²⁴, this would imply that the sky regions surveyed by these telescopes are systematically brighter than the average sky sampled with *HEAO-1* and *BeppoSAX* PDS. Another possible origin of the highest 2–10 keV CXB estimates could be due to systematic errors in the response function used for the diffuse emission (e.g., an underestimate of the stray light). In the case of MECS, this function could be well tested and cross-calibrated with the PDS only for point-like sources (see SI).

Independently of the CXB intensity issue at lower energies, our observational findings bear at least two important astrophysical consequences. Firstly, they provide a robust estimate of the accretion driven power integrated over cosmic time, including that produced by the most obscured AGNs. The AGN synthesis models, tuned to attain the PDS CXB level and to account for the hard

X-ray spectral shape^{3,25}, predict that at the bright fluxes ($> 10^{12}$ erg cm² s⁻¹) reachable by the PDS observations and by coded mask instruments like *INTEGRAL* IBIS and *Swift* BAT, the detectable fraction of extremely obscured AGNs (Compton thick, $N_H > 10^{24}$ cm²) is 10%, and it increases to 20–25% at the fluxes reachable by focusing telescopes (e.g., Ref. 26). It should be noted that the highest CXB intensities claimed at low energies^{5,8,17} (see Table 1) would entail a much larger number (a factor 2–3) of Compton thick AGNs³, a prediction barely consistent with the present observational evidence. Our result implies a present black hole mass density of $3 \cdot 10^5 M \text{ Mpc}^{-3}$, using an admittedly uncertain bolometric correction of 30 for the 15–50 keV band and an efficiency of 0.1 in converting gravitational into radiation energy. This corresponds to a fraction of $6 \cdot 10^{-5}$ of all baryons being locked into the supermassive black holes, using a cosmic baryon density of $4 \cdot 10^{31}$ g cm⁻³ in accord with the "concordance" cosmology model.

Secondly, under the assumption that the *HEAO-1* spectral shape⁶ applies down to 2 keV, we find that the summed contribution of the observed X-ray source counts in the 2–10 keV band¹⁴ exceeds the PDS CXB best fit level by 11%. This apparent contradiction vanishes if one takes into account the the above discussed upper limit in the PDS CXB intensity level and the error (7%) associated with the source count evaluation¹⁴. As a consequence our measurement suggests that it is quite possible that almost all the CXB in the 3–8 keV band has already been resolved into sources down to the faintest fluxes of the *Chandra* deep fields. Any substantial contribution to the CXB from other classes of sources and diffuse WHIM should be confined at photon energies below 3 keV, as it has already been indicated in the case of star forming galaxies²⁷.

References

1. Setti, G. & Woltjer, L. Active Galactic Nuclei and the Spectrum of the X-ray Background. *Astron. & Astrophys.* **224**, L21 (1989).
2. Comastri, A., Setti, G., Zamorani, G. & Hasinger, G. The Contribution of AGNs to the X-ray Background. *Astron. & Astrophys.* **296**, 1 (1995).
3. Gilli, R., Comastri, A. & Hasinger, G. The synthesis of the cosmic X-ray background in the *Chandra* and XMM-Newton era. *Astron. & Astrophys.* In press (astro-ph/0610939).
4. Revnivtsev, M., Gilfanov, M., Jahoda, K. & Sunyaev, R. Intensity of the Cosmic X-ray Background from HEAO1/A2 Experiment. *Astron. & Astrophys.* **444**, 381 (2005).

5. Hickox, R. C. & Markevitch, M. Absolute Measurement of the Unresolved Cosmic X-ray Background in the 0.5-8 keV Band with Chandra. *Astrophys. J.* **645**, 95 (2006).
6. Gruber, D. E., Matteson, J. L., Peterson, L. E. & Jung, G. V. The Spectrum of Diffuse Cosmic Hard X-Rays Measured with HEAO 1. *Astrophys. J.* **520**, 124 (1999).
7. Ueda, Y., Akiyama, M., Ohta, K. & Miyaji, T. Cosmological Evolution of the Hard X-Ray Active Galactic Nucleus Luminosity Function and the Origin of the Hard X-Ray Background. *Astrophys. J.* **598**, 886 (2003).
8. De Luca, A. & Molendi, S. The 2–8 keV Cosmic X-ray Background Spectrum as Observed with XMM-Newton. *Astron. & Astrophys.* **419**, 837 (2004).
9. Comastri, A. The Missing X-ray Background. In Mujica, R. & Maiolino, R. (eds.) *Multi-wavelength AGN Surveys*, 323 (Singapore: World Scientific Publishing Company, 2004).
10. Worsley, M. A. *et al.* The unresolved hard X-ray background: the missing source population implied by the Chandra and XMM-Newton deep fields. *Mon. Not. R. Astron. Soc.* **357**, 1281 (2005).
11. Ballantyne, D. R., Everett, J. E. & Murray, N. Connecting Galaxy Evolution, Star Formation, and the Cosmic X-ray Background. *Astrophys. J.* **639**, 740 (2006).
12. Hopkins, P. F. *et al.* A Unified, Merger-driven Model of the Origin of Starbursts, Quasars, the Cosmic X-Ray Background, Supermassive Black Holes, and Galaxy Spheroids. *Astrophys. J. Suppl.* **163**, 1 (2006).
13. Worsley, M. A. *et al.* Can the unresolved X-ray background be explained by emission from the optically-detected faint galaxies of the GOODS project. *Mon. Not. R. Astron. Soc.* **368**, 1735 (2006).
14. Moretti, A., Campana, S., Lazzati, D. & Tagliaferri, G. The Resolved Fraction of the Cosmic X-Ray Background. *Astrophys. J.* **588**, 696 (2003).
15. Horstman, H. M., Cavallo, G. & Moretti-Horstman, E. The X and Gamma Diffuse Background. *Rivista Nuovo Cimento* **5**, 255 (1975).
16. Marshall, F. E. *et al.* The Diffuse X-ray Background Spectrum from 3 to 50 keV. *Astrophys. J.* **235**, 4 (1980).

17. Vecchi, A., Molendi, S., Guainazzi, M., Fiore, F. & Parmar, A. N. The BeppoSAX 1–8 keV Cosmic Background Spectrum. *Astron. & Astrophys.* **349**, L73 (1999).
18. Lumb, D. H., Warwick, R. S., Page, M. & De Luca, A. X–ray Background Measurements with XMM-Newton EPIC. *Astron. & Astrophys.* **389**, 93 (2002).
19. Kuntz, K. D., Snowden, S. L. & Mushotzky, R. F. X-Ray Constraints on the Warm-Hot Intergalactic Medium. *Astrophys. J.* **548**, L119 (2001).
20. Frontera, F. *et al.* The High Energy Instrument PDS on-board the BeppoSAX X–ray Astronomy Satellite. *Astron. & Astrophys. Suppl. Ser.* **122**, 357 (1997).
21. Kushino, A. *et al.* Study of the X–Ray Background Spectrum and Its Large-Scale Fluctuation with ASCA. *Publ. Astron. Soc. Jpn.* **54**, 327 (2002).
22. Revnivtsev, M., Gilfanov, M., Sunyaev, R., Jahoda, K. & Markwardt, C. The Spectrum of the Cosmic X–ray Background Observed by RTXE/PCA. *Astron. & Astrophys.* **411**, 329 (2003).
23. A recent, still submitted *INTEGRAL* measurement (astro-ph/0608250) seems to be in agreement with our result.
24. Barcons, X., Mateos, S. & Ceballos, M. T. On the Intensity of the Extragalactic X–ray Background. *Mon. Not. R. Astron. Soc.* **316**, L13 (2000).
25. La Franca, F. *et al.* The HELLAS2XMM Survey. VII. The Hard X–Ray Luminosity Function of AGNs up to $z = 4$: More Absorbed AGNs at Low Luminosities and High Redshifts. *Astrophys. J.* **635**, 864 (2005).
26. Ferrando, P. *et al.* Simbol-X: mission overview. In Turner, M. & Hasinger, G. (eds.) *Space Telescopes and Instrumentation II: Ultraviolet to Gamma Ray. Proceedings of the SPIE, Volume 6266*, 11 (2006).
27. Ranalli, P., Comastri, A. & Setti, G. The 2–10 keV luminosity as a Star Formation Rate indicator. *Astron. & Astrophys.* **399**, 39 (2003).
28. Kirsch, M. G. *et al.* Crab: the standard X–ray candle with all (modern) X–ray satellites. In Siegmund, O. H. W. (ed.) *Proceedings of the SPIE, Volume 5898*, 22 (2005).
29. Zombeck, M. V. *Handbook of Space Astronomy and Astrophysics* (Cambridge University Press, 1990).

30. Kinzer, R. L., Johnson, W. N. & Kurfess, J. D. A balloon observation of the diffuse cosmic X–radiation above 20 keV. *Astrophys. J.* **222**, 370 (1978).
31. Jahoda, K. & et al. (2006). In preparation (available online at http://lheawww.gsfc.nasa.gov/users/keith/a2_cxb_15dec2005.pdf).
32. McCammon, D., Burrows, D. N., Sanders, W. T. & Kraushaar, W. L. The soft X–ray diffuse background. *Astrophys. J.* **269**, 107 (1983).
33. Georgantopoulos, I., Stewart, G. C., Shanks, T., Boyle, B. J. & Griffiths, R. E. A Deep ROSAT Survey — V. The Extragalactic Populations at Faint Fluxes. *Mon. Not. R. Astron. Soc.* **280**, 276 (1996).
34. Chen, L.-W., Fabian, A. C. & Gendreau, K. C. ASCA and ROSAT observations of the QSF3 field: the X-ray background in the 0.1-7 keV band. *Mon. Not. R. Astron. Soc.* **285**, 449 (1997).
35. Gendreau, K. C. *et al.* ASCA Observations of the Spectrum of the X–Ray Background. *Publ. Astron. Soc. Jpn.* **47**, L5 (1995).
36. Jung, G. V. The hard X–ray to low-energy gamma-ray spectrum of the Crab Nebula. *Astrophys. J.* **338**, 972 (1989).

Acknowledgements We wish to thank L. Bassani and A. Fabian for useful suggestions. *BeppoSAX* was a joint program of the Italian Space Agency (ASI) and the Netherlands Agency for Aerospace Programs. This research was supported by ASI and Ministry of Education, University and Research of Italy (COFIN 2002 and 2004).

Competing Interests The authors declare that they have no competing financial interests.

Correspondence Correspondence and requests for materials should be addressed to F.Frontera (email: frontera@fe.infn.it).

Table 1: Comparison of the past CXB measurements and their flux scale calibrations with Crab. When not available in the quoted papers, the Crab flux is taken from Kirsch et al. ²⁸. At low energies (1–15 keV), it is apparent a low spread of the PL photon index and a high spread (up to 40%) of the CXB intensity, exemplified by the ratio $R_{\text{HEAO } 1}^{2-10 \text{ keV}}$ between the measured 2–10 keV intensity and that measured with *HEAO-1* ($I_{\text{HEAO } 1}(2-10 \text{ keV}) = (5.41 \pm 0.08) \times 10^8 \text{ erg cm}^{-2} \text{ s}^{-1} \text{ sr}^{-1}$, Ref. 6). The highest intensities are those obtained with the focusing telescopes aboard *BeppoSAX*, *XMM-Newton* and *Chandra*. The ratio (= 1.15) obtained for the measurement with the collimated *Proportional Counter Array* aboard *Rossini-XTE* ²², and that (= 1.19) obtained from the re-analysis of the *HEAO-1* A2 measurement ⁴ can be lowered to 1.04 and 1.07, respectively, by a more reasonable calibration of the flux scale. Indeed the 2–10 keV Crab flux adopted ²⁹ is 11% higher than the mean value of all other Crab flux estimates. In the 20–50 keV energy band, the few available measurements show a low spread of the ratio $R_{\text{HEAO } 1}^{20-50 \text{ keV}}$ ($I_{\text{HEAO } 1}(20-50 \text{ keV}) = (6.06 \pm 0.06) \times 10^8 \text{ erg cm}^{-2} \text{ s}^{-1} \text{ sr}^{-1}$, Ref. 6), but systematic errors in the CXB intensity estimates cannot be excluded. In square parenthesis the values kept constant in the fits. Uncertainties are 1 σ errors for a single parameter. Where not reported, the uncertainties are very small or are not reported in the quoted papers.

10

Instrument	Ref.	Energy band (keV)	Model	kT or E _c (keV)	$R_{\text{HEAO } 1}^{2-10 \text{ keV}}$	$R_{\text{HEAO } 1}^{20-50 \text{ keV}}$	$F_{\text{Crab}}^{2-10 \text{ keV}}$ ($10^8 \text{ erg cm}^{-2} \text{ s}^{-1}$)	$F_{\text{Crab}}^{2-10 \text{ keV}}$ ($10^9 \text{ erg cm}^{-2} \text{ s}^{-1}$)
Composite	15	1–20	PL ^a	1:59 0:02	–	1.07	–	no data
Composite	15	20–200	PL ^a	2:040 0:013	–	–	0:86 0:05	no data
Balloon	30	20–165	PL ^a	2:17 0:07	–	–	0:90 0:18	no data
HEAO-1/A2	16	3–50	BREMSS ^b	–	[40]	0:98 0:10	0:92 0:05	no data
HEAO-1/A2	4	2–10	PL ^a	[1.4]	–	1:19 0:06	–	2.38
HEAO-1/A2	31	2–10	PL ^a	[1.558] ^c	–	1:05 0:06	–	2.29
HEAO-1/A2+ A4	6	3–60	CUTOFFPL ^d	1:29 0:02	41:13 0:62	1	1	no data
Rocket	32	2–6	PL ^a	[1.4]	–	1:34 0:21	–	2:29 0:10
ROSAT/SPSP	33	0.7–2.4	PL ^a	1:50 0:09	–	1:20 0:05	–	no data
ROSAT/SPSP	19	1.05–2.04	PL ^a	[1.46]	–	1:05 0:09	–	no data
ROSAT+ ASCA/SIS	34	1–7	PL ^a	1:48 0:07	–	1:12 0:04	–	2.16
SAX/MECS	17	1–8	PL ^a	1:40 0:04	–	1:43 0:08	–	1.97
ASCA/SIS	35	1–7	PL ^a	1:41 0:03	–	1:06 0:05	–	2.16
ASCA/GIS	21	1–10	PL ^a	[1.4]	–	1:18 0:02	–	2.16
XMM/EPIC-MOS/PN	18	2–8	PL ^a	1:42 0:03	–	1:30 0:14	–	1.90
RXTE/PCA	22	3–20	PL ^a	1:42 0:02	–	1:15 0:02	–	2.38
XMM/EPIC-MOS	8	2–8	PL ^a	1:41 0:06	–	1:36 0:10	–	1.90
Chandra/ACIS-I	5	2–8	PL ^a	[1.4]	–	1:33 0:13	–	1.95

^a PL model: $I(E) / E \text{ photons cm}^{-2} \text{ s}^{-1} \text{ keV}^{-1} \text{ sr}^{-1}$

^b The best fit was obtained with two PL plus a CUTOFFPL plus two edges.

^c Bremsstrahlung as described in the XSPEC user manual where kT is the plasma temperature.

^d $I(E) / E \exp(-E/E_c) \text{ photons cm}^{-2} \text{ s}^{-1} \text{ keV}^{-1} \text{ sr}^{-1}$

^e Estimate obtained with *HEAO-1* A4 ³⁶.

Table 2: Results of the fits to the spectrum $D(E)$ with the difference between the CXB spectrum and that of the albedo from the dark Earth. For the CXB, only total (resolved plus unresolved) normalizations N_{CXB} are reported. For the albedo spectrum, we used a photo-electrically absorbed PL model $I_{\text{A}}(E) = \exp(-t_{\text{A}}/A)N_{\text{A}}(E=20)^{-\alpha}$ photons $\text{cm}^{-2} \text{s}^{-1} \text{keV}^{-1} \text{sr}^{-1}$, where N_{A} is the normalization constant at 20 keV, A is the air absorption coefficient in units of cm^2/g , and t_{A} is atmospheric depth that describes the well known cutoff in the albedo spectrum (see SI). To model the CXB spectrum we assumed the broad band CXB spectral shape obtained with *HEAO-1* A2+ A4⁶. Thus we used as input models a CUTOFFPL and a PL, which in the 15–50 keV still gives a good description of this shape. The parameters that were left free in the single fits are those reported with their uncertainties. We explored in different fits the entire space of all parameters that were frozen in the single fits (shown in square brackets), except for the cutoff energy E_{c} which was always frozen to the value of 41.13 keV found with *HEAO-1* (see Table 1). Indeed, given our energy band (15–50 keV), our fits were insensitive to E_{c} . A and t_{A} were varied in the range 1.3–2.0 and 1.4–6, respectively, to cover the values found in past measurements (see SI). The CXB photon index γ was varied in the range 1.9 to 2.1 for the PL, and in 1.2 to 1.4 for the CUTOFFPL. For wider ranges, the results do not significantly change (see SI). The reported parameter values and the derived CXB 20–50 keV integrated intensity $I^{20-50 \text{ keV}}$ are the most likely in the parameter space and minimize the χ^2 (see details in SI). The quoted uncertainties are errors at 90% confidence level for a single parameter.

Model	$N_{\text{CXB}}^{\text{a}}$	E_{c}^{b}	$I_{\text{A}}(20 \text{ keV})^{\text{a}}$	A	t_{A}^{e}	γ	$I^{20-50 \text{ keV}}$
Power-law ^c	0.100 ± 0.003 [1.98]		0.014 ± 0.002 [1.38]	[1.91]	9.43/23	5.89 ± 0.31	
Cutoff power-law ^d	0.158 ± 0.005 [1.4]	[41.13]	0.011 ± 0.001 [1.53]	[2.42]	9.2/23	5.52 ± 0.31	
Cutoff power-law ^d	0.167 ^{+0.039} _{0.017}	1.4 ^{+0.4} _{0.6} [41.13]	0.011 ^{+0.015} _{0.006}	[1.3]	[1.4]	9.0/22	5.88 ± 0.32
Cutoff power-law ^d	0.148 ± 0.004 [1.29]	[41.13]	0.0040 ± 0.0004 [2.0]	[4.98]	9.2/23	5.43 ± 0.29	

^a In units of photons $\text{cm}^{-2} \text{s}^{-1} \text{keV}^{-1} \text{sr}^{-1}$

^b In units of keV

^c $I_{\text{CXB}}(E) = N_{\text{CXB}}(E=20)$

^d $I_{\text{CXB}}(E) = N_{\text{CXB}}(E=20) \exp(-E/E_{\text{c}})$

^e In units of g cm^{-2}

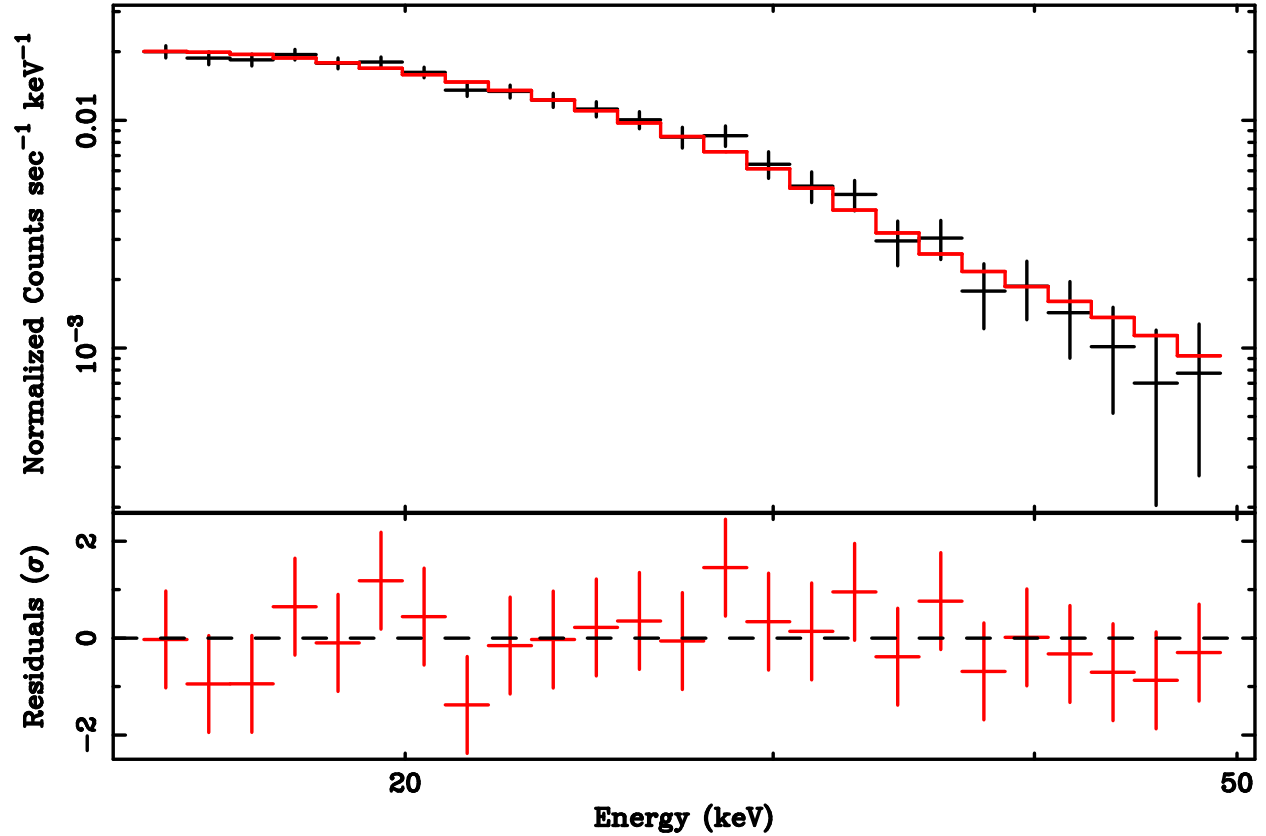


Figure 1: *Top panel*: Average difference spectrum $D = C_{\text{X B}} - A$ of all the available data, along with one of the best fit models. In this case the CXB spectrum is modeled with a PL and the terrestrial albedo with an absorbed PL (see text). *Bottom panel*: residuals to the model.

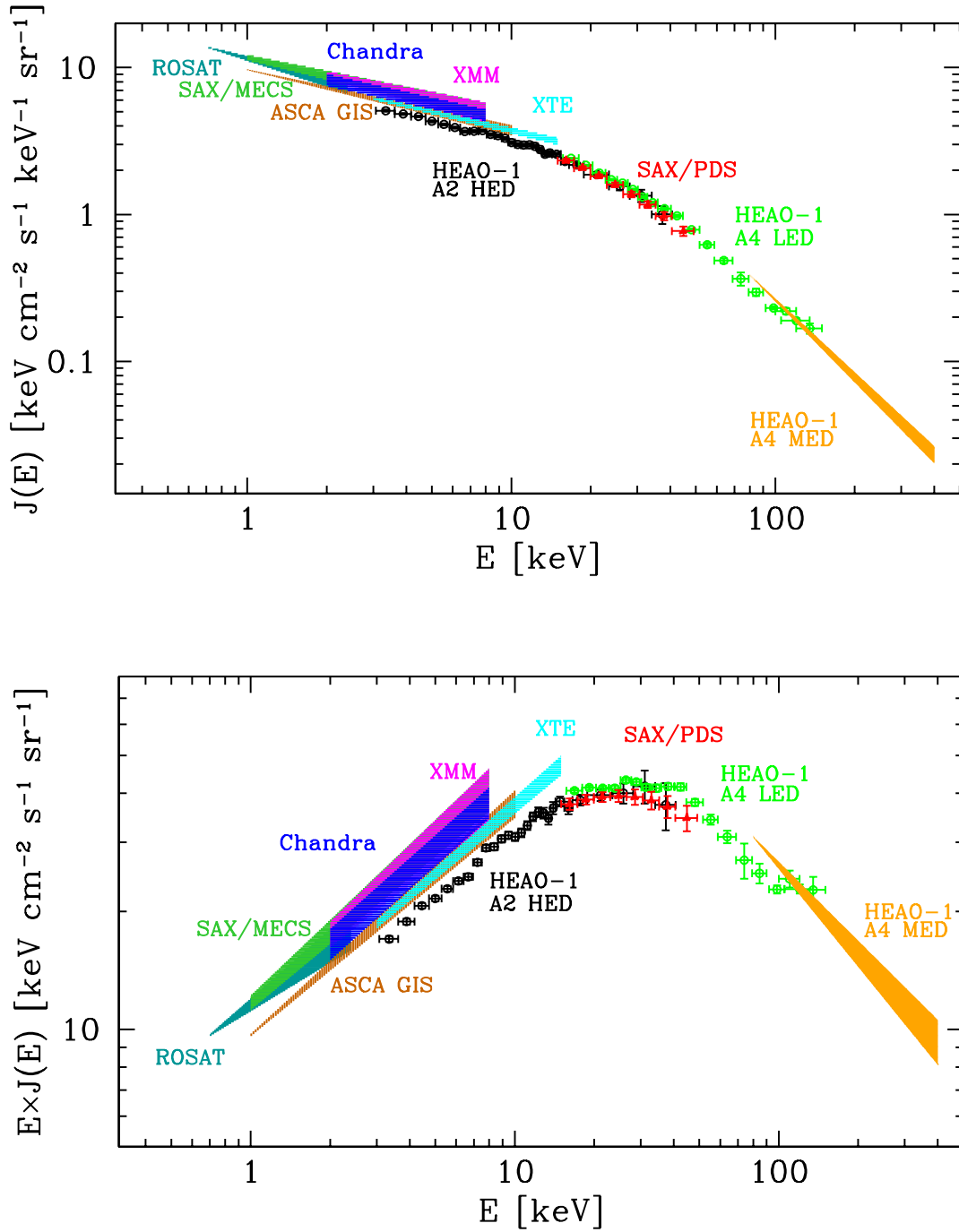


Figure 2: Total (unresolved plus resolved) CXB spectrum as observed with the PDS experiment (red points) compared with measurement results obtained with other missions. *Upper panel:* The energy spectrum $J(E)$ modeled with a CUTOFFPL with $\alpha = 1.4$ (see Table 2 and E_c fixed at the value of 41.13 keV obtained with *HEAO-1* A2+A4⁶). *Bottom panel:* The $E J(E)$ spectrum modeled with the same CUTOFFPL as above. The fitting parameters are listed in Table 2.

Supplementary Information for the paper “How large is the population of heavily obscured X-ray sources?”

1 PDS response function and solid angle, and their calibration with the Crab Nebula

The ON-axis PDS response function was determined by means of pre-launch calibrations combined with Monte Carlo calculations, and it was tested in flight with several repeated observations of the Crab Nebula. Indeed, during the *BeppoSAX* life time (6 yrs), seven observations of the Crab Nebula (two in 1997, one in 1998, two in 1999, one in 2000, and one in 2001) were performed to calibrate the Narrow Field Instruments (NFIs) aboard the satellite. Assuming a power-law (PL) model ($I(E) = N E^{-\Gamma}$ photons $\text{cm}^{-2} \text{s}^{-1} \text{keV}^{-1}$), the photon index Γ obtained with the PDS remained unchanged in all of these observations within the statistical uncertainties, with a mean value of 2.121 ± 0.001 , and a reduced $\chi^2 = 25.5$ for 66 degrees of freedom (dof), in the 15–200 keV band. A better fit ($\chi^2_{\text{dof}} = 17.1$ for 64 dof) in this energy band was obtained with a broken power-law (BKNPL), with a mean low energy index $\Gamma_1 = 2.113 \pm 0.001$, a break energy $E_b = 74 \pm 2$ keV, and a high energy index $\Gamma_2 = 2.198 \pm 0.005$. A BKNPL spectrum was also the best fit to other broad band high energy measurements (see, e.g., Ref. 1). The still high χ^2_{dof} obtained with the BKNPL model can be lowered and made compatible with the χ^2 statistics if a systematic error of 1% in the used PDS response function is assumed.

A cross-calibration of the *BeppoSAX* PDS and MECS telescopes (see, e.g., Ref. 2), performed with Crab, has provided a time averaged normalization ratio between PDS and MECS of $R(\text{PDS}=\text{MECS}) = 0.928 \pm 0.001$ in the assumption of a PL model, and 0.917 ± 0.001 in the assumption of a BKNPL. When corrected for this normalization ratio, the mean value of the above PL normalization parameter (in units of photons $\text{cm}^{-2} \text{s}^{-1} \text{keV}^{-1}$ at 1 keV) $N = 9.54 \pm 0.01$, while, for a BKNPL, $N = 9.39 \pm 0.02$. A comparison of this Crab spectrum with that obtained with other instruments (see Fig. 1) shows that the so derived PDS spectrum is consistent within 8% with the extrapolation of the 0.3–10 keV spectrum obtained with the *XMM-Newton* EPIC–MOS camera³, with the Crab spectrum obtained with *HEAO-1 A4*⁴, with the mean value of Crab spectrum quoted by Kirsch et al.⁵ and with the classical Toor & Seward⁶ results. As can also be seen from Fig. 1, with respect to the Crab 15–50 keV spectrum obtained with the PDS, that quoted by Zombeck⁷ is higher by 30%, while that reported by Bartlett¹ is lower by 15%.

The OFF-axis response function of the PDS was tested with the Crab Nebula during the *BeppoSAX* Science Verification Phase. The Crab was observed in September 1996 at different offset

angles with respect to the instrument axis pointing and with a roll angle such to get the narrowest angular response of the hexagonal collimators. While preliminary results were reported ⁸, in Fig. 2 we show the angular response of each PDS unit to Crab in the 15–100 keV band. The fit of the data was performed assuming a triangular response, as expected from the collimator design. As it can be seen, the derived Full Width at Half Maximum θ_{FW} ($= 1.32^\circ$) is fully consistent with that derived in the pre-flight tests ⁹. The result is that the response function is independent of the offset angle θ apart from the exposed area through the collimators, which linearly decreases with θ .

The solid angle of the PDS is derived from the Geometric Factor of the telescope defined as ^{10,11}

$$G = \int_{\Omega} A(\theta) d\Omega; \quad (1)$$

where $A(\theta)$ is the exposed detector geometric area through the collimators at an offset angle θ , and Ω is the solid angle of the instrument Field of View (FOV). The expression of G , for an hexagonal collimator like that of the PDS, can be found in Ref. 11 and is given by

$$G = A(0) \tan^2 \left(0.5 \tan^{-1} \frac{0.93939 d_m}{h} \right) \quad (2)$$

where $A(0)$ is the ON-axis geometric area through the collimator (640 cm^2), d_m is the diameter of the circumscribed circle to the hexagonal collimator cells, and h is collimator height. The ratio d_m/h is related to the minimum FWHM of the angular response of the PDS θ_{FW} through the relation

$$\frac{d_m}{h} = \frac{2}{\sqrt{3}} \tan \theta_{FW} \quad (3)$$

Using the value of θ_{FW} derived from the offset Crab observations, we obtain a value of $G = 0.295 \text{ cm}^2 \text{ sr}$, and, dividing by $A(0) = 640 \text{ cm}^2$, we find the telescope solid angle $\Omega = 4.624 \cdot 10^{-4} \text{ sr}$.

2 Methods adopted by HEAO-1 A2 and A4 experiments to measure the CXB spectrum

In the case of the HEAO-1 A2 experiment, the total background level B_{sky} measured during the observation of a blank sky field ($B_{sky} = C_{XB} + B_{in}$, where C_{XB} is the CXB count rate entering through telescope FOV and B_{in} is the intrinsic background) was simultaneously observed through two collimators with different FOVs, one with a solid angle twice that of the other. Assuming B_{in} to be independent of the instrument FOV, the difference between the two total background levels removes the intrinsic background and gives directly C_{XB} (see Ref. 12, hereafter M80).

In the case of the *HEAO-I* A4 experiment^{13,14}, the unresolved CXB spectrum was derived by subtracting from the B^{sky} , measured when the detectors observed blank sky fields, the background measured when the FOV of the detectors was shielded with a shutter made of a scintillator detector in anti-coincidence with the main detectors.

In both cases a biased estimate of C_{XB} cannot be excluded given that the intrinsic background is dependent on the mass exposed to the environmental radiation: in the first case, we have different collimator apertures, while, in the second case, the shutter could modify the intrinsic background.

3 Selection of blank sky fields

Great care was devoted to the selection of blank sky fields. We discarded those pointings within 15° from the Galactic plane, in order to avoid contamination from the population of bright Galactic sources and from the Galactic diffuse emission. The complete list of the selected fields can be found elsewhere¹⁵. In addition, for the OFF-source pointings we filtered out those observations for which the +OFF and OFF fields could be contaminated, e.g., from serendipitous X-ray sources, fast transients or solar flares. This selection was done by excluding from the sample those observations for which the difference between the two offset spectra (+OFF minus OFF) were inconsistent with zero at 98% confidence level. For the ON-source pointings we accepted only those fields for which the difference between the ON-source count rate and count rate measured at either +OFF and OFF is consistent with zero within 1σ , and for which a fit with a null constant to the difference between the corresponding offset spectra (+OFF minus OFF) gives a χ^2 per degree of freedom in the range 0.8–1.2. All the sky observations were done only when the instrument axis pointed at a direction at least 5° away from the Earth limb.

4 Difference spectra

We obtained three difference spectra: one ($D_{\text{ON}}(E)$) for the ON-source pointings (2350 ks of exposure time), another ($D_{+\text{OFF}}(E)$) for the +OFF-source pointings (800 ks), and the third ($D_{\text{OFF}}(E)$) for the OFF-source pointings (881 ks). They are shown in Fig. 3. As can be seen, all are consistent with each other, within their uncertainties, as also confirmed with a run test¹⁶. The small observed deviations from each other give an indication of the systematic errors made in the estimate of the difference $B_{\text{in}}^{\text{sky}} - B_{\text{in}}^{\text{Earth}}$. However the results from the offset and ON-source pointings

agree within the statistical errors.

On the basis of these results, for the derivation of the CXB intensity we used the sum $D(E) = D_{\text{ON}}(E) + D_{+\text{OFF}}(E) + D_{-\text{OFF}}(E)$ which is determined up to 50 keV and is shown in Fig. 1 of the main paper. When $D(E)$ is fit with a PL model, we find an unacceptable $\chi^2/\text{dof} (= 37.4/23)$ in the 15–50 keV band, and a better value ($= 15.5/16$) in the 20–50 keV band. However, also in this case, the best fit PL photon index at 90% confidence level (3.2 ± 0.2) is much higher than that expected for the CXB (see Table 1 of the main paper). We infer that $D(E)$ does not give the CXB spectrum but, as expected, the difference spectrum between CXB and albedo from the dark Earth. As also found with numerical simulations, the derived photon index unambiguously shows that the mean slope of albedo spectrum is harder than that of the CXB.

5 The albedo spectrum

The terrestrial gamma-ray albedo radiation is mainly the result of the interactions with upper atmosphere of the Cosmic-Rays and, at X-ray energies, of the CXB and of the discrete X-ray source radiation (Compton reflection). It was investigated since the late 1960s (see, e.g., review by Peterson¹⁷). Most of the properties of the atmospheric gamma-rays were obtained with balloon experiments, mainly launched from Palestine (Texas, USA). Empirical models of the atmospheric gamma-ray emission, based on observational results, were worked out by various authors^{17–19}. From these observations, it can be seen that the gamma-ray emission properties depend on various parameters, like the geomagnetic latitude, the energy band, the direction of emission (downward, upward), the altitude from the Earth. Also the atmospheric radiation measured by a satellite depends on these parameters, but, unlike the radiation observed by a balloon experiment, a satellite observes only the radiation emerging from the top of the atmosphere (albedo radiation). Thus its spectral properties, specially at low energies (> 10 keV), are expected to be different from those observed inside the atmosphere. Measurements of the X-ray albedo radiation are reported in Ref. 20 for photon energies in the 10–300 keV band, and in Ref. 21 above 40 keV, while for energies higher than 150 keV (see, e.g., Refs. 19, 22).

The albedo spectrum of Ref. 20, which was obtained with a 0.5 cm scintillator detector and a wide FOV (23° at zero response) aboard the *OSO-3* satellite in a nearly circular orbit at an inclination of 33° and an altitude of 550 km²³, above 40 keV is consistent with a PL (see Fig. 4), while below 40 keV it shows a flattening with a definitive low energy cutoff below 30 keV. This cut-off is also observed with balloon experiments^{10, 17, 20} and it is attributed to self-absorption

of the radiation emitted from inner and inner atmospheric layers. The PL model above 40 keV is confirmed by the albedo spectrum measured with a 50 cm³ Ge(Li) cooled detector with a wide FOV as well ($\approx 45^\circ$ at zero response) aboard the low–altitude polar–orbiting satellite *1972–076B*²¹ (see Fig. 4).

Following Schwartz²⁴, the best fit to the > 10 keV albedo spectrum measured with *OSO–3* is obtained with a photo-electrically absorbed PL $I_A(E) = \exp(-\tau_A) N_A (E=20)^{-\alpha}$ photons cm^{–2} s^{–1} keV^{–1} sr^{–1}, with photon index $\alpha = 1.7 \pm 0.3$, and atmospheric thickness $\tau_A = 1.75 \pm 0.15$ g/cm² (at 90% confidence level). In the case of the polar–orbiting satellite, Imhof et al.²¹ found that above 40 keV the photon spectrum is consistent with a PL with index ranging from 1.34 to 1.39, depending on the latitude scanned²¹.

On the basis of these observation results, we have assumed a photo-electrically absorbed PL as model spectrum for the albedo radiation from the dark Earth. To describe the low–energy cutoff, we developed an atmospheric absorption model within the XSPEC software package²⁵, that we adopted for our model fitting. The model makes use of a grid of values of air mass X–ray attenuation coefficients as a function of the photon energy²⁶. In the model fit we left to vary the atmospheric depth τ_A (in units of g cm^{–2}) in the range 1.4–6 that includes the values obtained with *OSO–3*, and the PL photon index α in the range 1.3–2.0, which includes the values measured with both *OSO–3* and *1972–076B* and takes into account the fact that the albedo mean slope is harder than that of the CXB, as demonstrated above (see section 4).

The best fit results of the albedo photo-electrically absorbed PL are reported in the Table 1 of the main paper. In Fig. 4 we show our best fit spectrum of the albedo from the dark Earth. As can be seen, it is located between the *OSO–3* results and the albedo spectrum derived by Imhof et al.²¹, with a 20–50 keV integrated intensity of $(8 \pm 2) \times 10^{10}$ erg cm^{–2} s^{–1} sr^{–1}. Apart from the fact that we have measured this intensity during the dark Earth, it should be noticed that the intensity of the albedo radiation depends on the CR flux hitting the Earth, and thus on magnetic latitude. Given that in different Earth pointings we pointed to the Earth along generally different directions and thus to different magnetic latitudes, the derived spectrum is latitude averaged, as partially done also in the case of the *OSO–3* and *1972–076B* satellites due to their wide FOVs. We also notice that at different latitudes we do not observe the upward albedo, but the albedo emerging at different zenith angles Z . However, as discussed by Ling¹⁸, the atmospheric spectrum at low energies is expected to be not strongly anisotropic with Z .

6 Contribution of resolved sources to the 15–50 keV CXB intensity

Exploiting the PDS pointings, we also performed an estimate of the contribution of resolved sources to the 15–50 keV integrated CXB intensity. This estimate could not be done using the ON-source pointings of the PDS, given that most of them were pointed observations of specific targets by the *BeppoSAX* Narrow Field Instruments (NFI) LECS, MECS, HPGSPC, and PDS. However, in 33 of the PDS OFF-source fields, significant count excesses (3–7 σ), consistent with the presence of serendipitous X-ray sources, were found. The spectra of these excesses, when fit with a PL model, gave a weighted mean value of their photon indices equal to 1.65 ± 0.20 , while their intensity gave a 15–50 keV energy flux in the range $(1.4\text{--}20) \times 10^{-12} \text{ erg cm}^{-2} \text{ s}^{-1}$, corresponding to 0.1–1.5 mCrab. A search of their counterparts is now in progress. Their contribution increases the CXB intensity by 4.7%.

7 Details on the derivation of our results and their comparison with the past CXB measurements

All the best fit parameter values, quoted with their uncertainties in Table 2 of the main paper, have been derived by taking into account their frequency distribution obtained by varying the value of all the other parameters that were frozen in the single fits. τ_A and t_A were varied in the range (1.3–2.0) and (1.4–6.0), respectively (see Section 5), while the CXB photon index Γ was varied in the range (1.9–2.1) or (1.2–1.4), depending on the assumed CXB model, a PL or a CUTOFFPL, respectively. (For wider ranges of Γ , see below).

In Figs. 6 and 7 (left panels) we show the frequency distribution of the 20–50 keV integrated intensity $I(20\text{--}50 \text{ keV})$ of the total CXB for a PL and CUTOFFPL model, respectively. These distributions were obtained by selecting the spectral solutions for which the PL photon index of the reconstructed $D(E)$ spectrum in the 20–50 keV band is in the range 2.9–3.5, consistently with the observed slope of $D(E)$ (see Sect. 4). (Without this constraint the peak of the distribution occurs at slightly lower values of $I(20\text{--}50 \text{ keV})$.)

As can be seen, the distribution is well peaked (also the distributions of the other best fit parameters show a similar shape), with peak values mainly corresponding to the peak of the χ^2 distribution (see right panel of Figs. 6 and 7). We have adopted as likely values of $I(20\text{--}50 \text{ keV})$ those around the maximum of the distribution and we considered as best fit parameter values (reported in Table 2 of the main paper) those that in a region around the maximum of the $I(20\text{--}50 \text{ keV})$

frequency distribution give the minimum χ^2 . Using the $I(20-50 \text{ keV})$ frequency distributions, we find that, independently of the CXB input model (see Table 1 and Table 2 of the main paper), 90% of the data points have a total CXB intensity $I(20-50 \text{ keV}) < 6.8 \times 10^{-8} \text{ erg cm}^{-2} \text{ s}^{-1} \text{ sr}^{-1}$. We assume this value as upper limit to our CXB estimate.

By increasing the range of the CXB photon index values to 1.8–2.2 for the PL, and to 1.1–1.5 for CUTOFFPL, we find similar $I(20-50)$ distributions with a peak at slightly lower intensity values but with upper limit almost unchanged with respect to that given above.

For the comparison with the past results, in addition to Fig. 2 of the main paper, we show in Fig. 5 the energy spectrum $J(E)$ and the $EJ(E)$ spectrum of the CXB in the case of the PL model. In Table 1 we compare the 20–50 keV CXB intensities derived from past measurements and those derived by us. The 20–50 keV flux from the Crab Nebula is also reported when available. As can be seen from this Table, our best estimates of the 20–50 keV integrated CXB intensity are nicely consistent with the *HEAO-1* A2 results¹². Instead, with respect to the CXB intensity derived from Gruber et al.¹³, that estimated with the PDS is lower by a value ranging from $\sim 10\%$ when both Γ and E_c of the CUTOFFPL model are frozen to those of Gruber et al.¹³ to a value of $\sim 3\%$ in the case the PL model and and in the case of the CUTOFFPL when both parameters are left free to vary in the single fits (see Table 1). We notice however that, in the case of *HEAO-1* A4, the flux scale calibration used⁴ is 6% higher than that used for the PDS. If we normalize that used by Gruber et al.¹³ to ours, also the *HEAO-1* A4 and PDS 20–50 keV intensity estimates become mutually consistent.

The upper limit derived above establishes that, at 90% confidence level in the entire multi-parameter space, the 20–50 keV CXB integrated intensity is 12% higher than that obtained from the Gruber et al.¹³ results and 21% than that obtained from the Marshall et al.¹² best estimate.

Finally, in Fig. 8 we show the amount of sky covered by the PDS compared with that covered by different focusing missions for the unresolved CXB determination.

References

1. Bartlett, L. M. *High Resolution Gamma-ray Spectroscopy of the Crab*. Ph.D. thesis, NASA/Goddard Space Flight Center (1994).

2. Boella, G. *et al.* The medium-energy concentrator spectrometer on board the BeppoSAX X-ray astronomy satellite. *Astron. & Astrophys. Suppl. Ser.* **122**, 327 (1997).
3. Willingale, R. *et al.* New Light on the X-ray Spectrum of the Crab Nebula. *Astron. & Astrophys.* **365**, L212 (2001).
4. Jung, G. V. The hard X-ray to low-energy gamma-ray spectrum of the Crab Nebula. *Astrophys. J.* **338**, 972 (1989).
5. Kirsch, M. G. *et al.* Crab: the standard X-ray candle with all (modern) X-ray satellites. In Siegmund, O. H. W. (ed.) *Proceedings of the SPIE, Volume 5898*, 22 (2005).
6. Toor, A. & Seward, F. D. The Crab Nebula as a Calibration Source for X-ray Astronomy. *Astron. J.* **79**, 995 (1974).
7. Zombeck, M. V. *Handbook of Space Astronomy and Astrophysics* (Cambridge University Press, 1990).
8. Frontera, F. *et al.* PDS Experiment on board the BeppoSAX Satellite: Design and in-flight Performance Results. *Proc. SPIE* **3114**, 206 (1997).
9. Frontera, F. *et al.* The High Energy Instrument PDS on-board the BeppoSAX X-ray Astronomy Satellite. *Astron. & Astrophys. Suppl. Ser.* **122**, 357 (1997).
10. Peterson, J. L., Schwartz, D. A. & Ling, J. C. Spectrum of Atmospheric Gamma Rays to 10 MeV at $\theta = 40^\circ$. *J. Geophys. Res.* **78**, 7942 (1973).
11. Horstman, H. M., Cavallo, G. & Moretti-Horstman, E. The X and Gamma Diffuse Background. *Rivista Nuovo Cimento* **5**, 255 (1975).
12. Marshall, F. E. *et al.* The Diffuse X-ray Background Spectrum from 3 to 50 keV. *Astrophys. J.* **235**, 4 (1980).
13. Gruber, D. E., Matteson, J. L., Peterson, L. E. & Jung, G. V. The Spectrum of Diffuse Cosmic Hard X-Rays Measured with HEAO 1. *Astrophys. J.* **520**, 124 (1999).
14. Kinzer, R. L., Jung, G. V., Gruber, D. E., Matteson, J. L. & Peterson, L. E. Diffuse Cosmic Gamma Radiation Measured by HEAO 1. *Astrophys. J.* **475**, 361 (1997).
15. Landi, R. *The Hard X-ray Sky off the Galactic Plane as seen by the BeppoSAX/PDS Experiment*. Ph.D. thesis, Physics Department, University of Bologna (2005).

16. Bendat, J. S. & Piersol, A. G. *Random data: Analysis and Measurement Procedures* (Wiley–Interscience, 1971).
17. Peterson, L. E. Instrumental Technique in X–ray Astronomy. *Ann. Rev. Astron. Astrophys.* **13**, 423 (1975).
18. Ling, J. C. A Semiempirical Model for Atmospheric Gamma Rays from 0.3 to 10 MeV at a Geomagnetic Latitude of 40 deg. *J. Geophys. Res.* **80**, 3241 (1975).
19. Dean, A. J., Fan, L., Byard, K., Goldwurm, A. & Hall, C. J. The gamma–ray emissivity of the earth’s atmosphere. *Astron. & Astrophys.* **219**, 358 (1989).
20. Schwartz, D. A. & Peterson, L. E. The Spectrum of Diffuse Cosmic X–Rays Observed by OSO–3 Between 7 and 100 KEV. *Astrophys. J.* **190**, 297 (1974).
21. Imhof, W. L., Nakano, G. H. & Reagan, J. B. High-resolution Measurements of Atmospheric Gamma Rays from a Satellite. *J. Geophys. Res.* **81**, 2835 (1976).
22. Letaw, J. R., Share, G. H., Kinzer, R. L., Silberberg, R. & Chupp, E. L. Measurement of gamma–ray line intensities from the earth’s atmosphere. *Adv. Space Res.* **6**, 133 (1986).
23. Schwartz, D. A., Hudson, H. S. & Peterson, L. E. The Spectrum of Diffuse Cosmic X–Rays 7.7–113 keV. *Astrophys. J.* **162**, 431 (1970).
24. Schwartz, D. A. . Ph.D. thesis, University of California at San Diego (1969).
25. Arnaud, K. A. XSPEC: The First Ten Years. *ASP Conf. Series* **101**, 17 (1996).
26. Hubbell, J. H. & Seltzer, S. M. (1996). Available online at <http://physics.nist.gov/PhysRefData/XrayMassCoef/cover.html>.
27. Kinzer, R. L., Johnson, W. N. & Kurfess, J. D. A balloon observation of the diffuse cosmic X–radiation above 20 keV. *Astrophys. J.* **222**, 370 (1978).
28. Vecchi, A., Molendi, S., Guainazzi, M., Fiore, F. & Parmar, A. N. The BeppoSAX 1–8 keV Cosmic Background Spectrum. *Astron. & Astrophys.* **349**, L73 (1999).
29. Kushino, A. *et al.* Study of the X–Ray Background Spectrum and Its Large-Scale Fluctuation with ASCA. *Publ. Astron. Soc. Jpn.* **54**, 327 (2002).
30. Lumb, D. H., Warwick, R. S., Page, M. & De Luca, A. X–ray Background Measurements with XMM-Newton EPIC. *Astron. & Astrophys.* **389**, 93 (2002).

31. Hickox, R. C. & Markevitch, M. Absolute Measurement of the Unresolved Cosmic X-ray Background in the 0.5-8 keV Band with Chandra. *Astrophys. J.* **645**, 95 (2006).
32. De Luca, A. & Molendi, S. The 2–8 keV Cosmic X-ray Background Spectrum as Observed with XMM-Newton. *Astron. & Astrophys.* **419**, 837 (2004).

Table 1: Comparison of our results with the past measurements. For each model, the parameters of the CXB photon spectrum and the corresponding 20–50 keV energy flux per steradian are reported. For flux scale calibration purposes, when available, also the 20–50 Crab flux predicted from the single experiments is reported. In the case of PDS, the normalization parameter N includes the contribution of the resolved sources. Uncertainties are 1σ errors. Parameters in square parenthesis are those kept fixed in the single fits.

Experiment	Ref.	Energy band (keV)	Model	N		kT or E_c (keV)		$F_{\text{CXB}}^{20-50\text{ keV}}$ (10^{-8} erg cm $^{-2}$ s $^{-1}$ sr $^{-1}$)		$F_{\text{Crab}}^{20-50\text{ keV}}$ (10^{-9} erg cm $^{-2}$ s $^{-1}$)	
Composite	11	20–200	PL ^a	40:7	2:3	2:040	0:013	—	5:2	0:3	NA
Balloon	27	20–165	PL ^a	67	13	2:17	0:07	—	5:47	1:06	NA
HEAO-1/A2	12	3–50	BREMSS ^b	13:95	0:70	—	—	[40]	5:6	0:3	NA
HEAO-1/A2+A4	13	3–60	CUTOFFPL ^c	7:877	0:08	[1.29]	—	[41.13]	6:06	0:06	9:83 0:03
SAX/PDS	this paper	15–50	PL ^d	0:100	0:002	[1.98]	—	—	5:89	0:19	9:22 0:01
SAX/PDS	this paper	15–50	CUTOFFPL ^e	0:158	0:03	[1.4]	—	[41.13]	5:52	0:18	9:22 0:01
SAX/PDS	this paper	15–50	CUTOFFPL ^e	0:167	0:017	1:4	0:3	[41.13]	5:88	0:19	9:22 0:01
SAX/PDS	this paper	15–50	CUTOFFPL ^e	0:148	0:002	[1.29]	—	[41.13]	5:43	0:17	9:22 0:01

$$^a I(E) = N E \text{ photons cm}^{-2} \text{ s}^{-1} \text{ keV}^{-1} \text{ sr}^{-1}$$

^b Bremsstrahlung as described in the XSPEC user manual with $N = K$ and kT is the plasma temperature.

$$^c I(E) = N E \exp(-E/E_c) \text{ photons cm}^{-2} \text{ s}^{-1} \text{ keV}^{-1} \text{ sr}^{-1}$$

$$^d I(E) = N (E=20) \text{ photons cm}^{-2} \text{ s}^{-1} \text{ keV}^{-1} \text{ sr}^{-1}$$

$$^e I(E) = N (E=20) \exp(-E/E_c) \text{ photons cm}^{-2} \text{ s}^{-1} \text{ keV}^{-1} \text{ sr}^{-1}$$

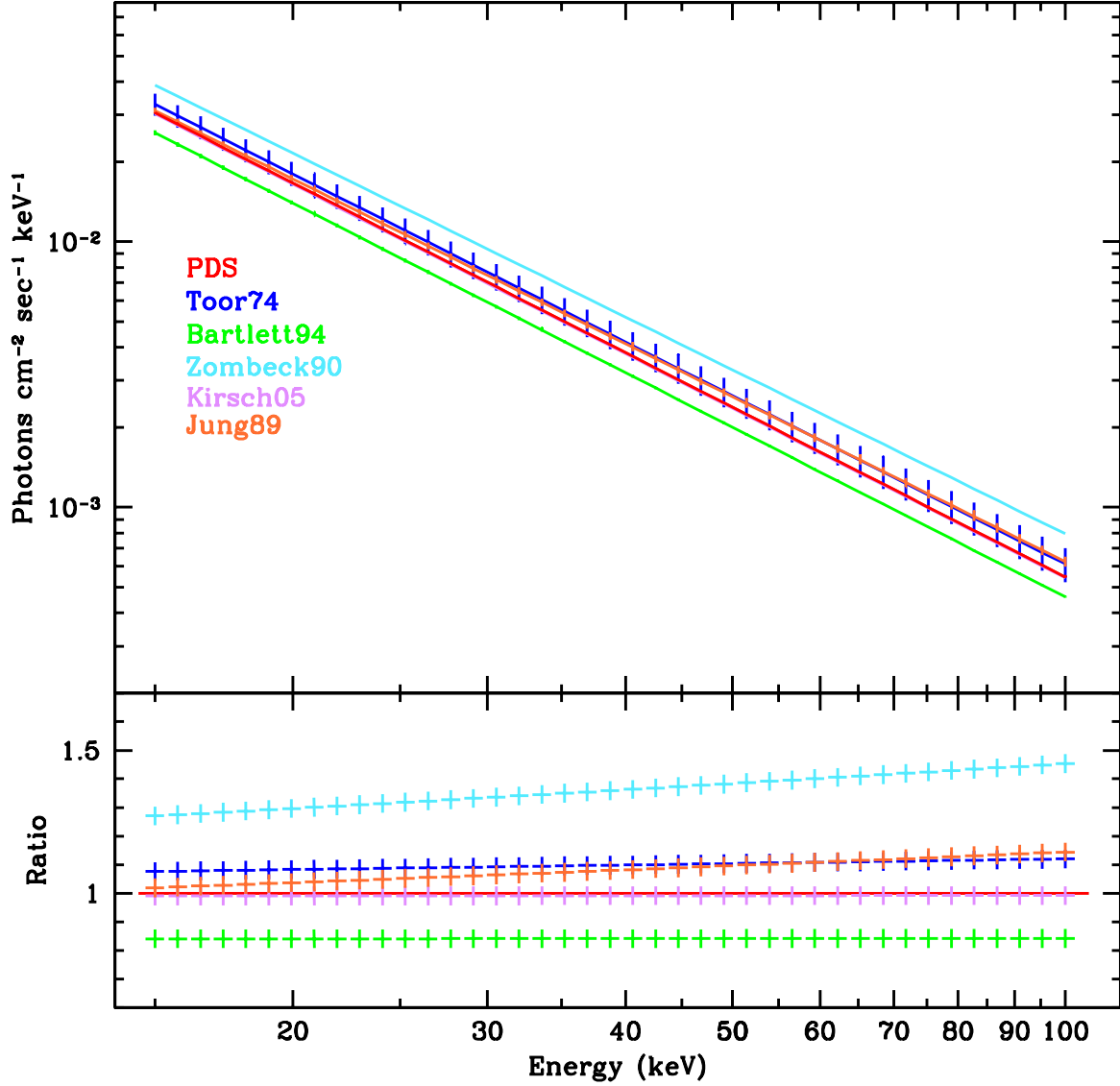


Figure 1: *Upper panel*: *BeppoSAX* 15–100 keV Crab spectrum (red points) compared with other measurements. *Blue line*: review of different measurements in 5–70 keV ⁶; *Green line*: GRIS balloon experiment in 20–1000 keV ¹; *Cyan line*: Zombeck ⁷; *Purple line*: collection of different measurements in 2–50 keV ⁵; *Orange line*: 15–180 keV *HEAO-1* A4/LED measurement ⁴. When not visible, error bars are smaller than the line thickness. *Bottom panel*: ratio between the Crab spectrum as measured by previous experiments and the PDS spectrum. With the exception of the Zombeck and the Bartlett measurements, all the others are consistent with each other within 8%.

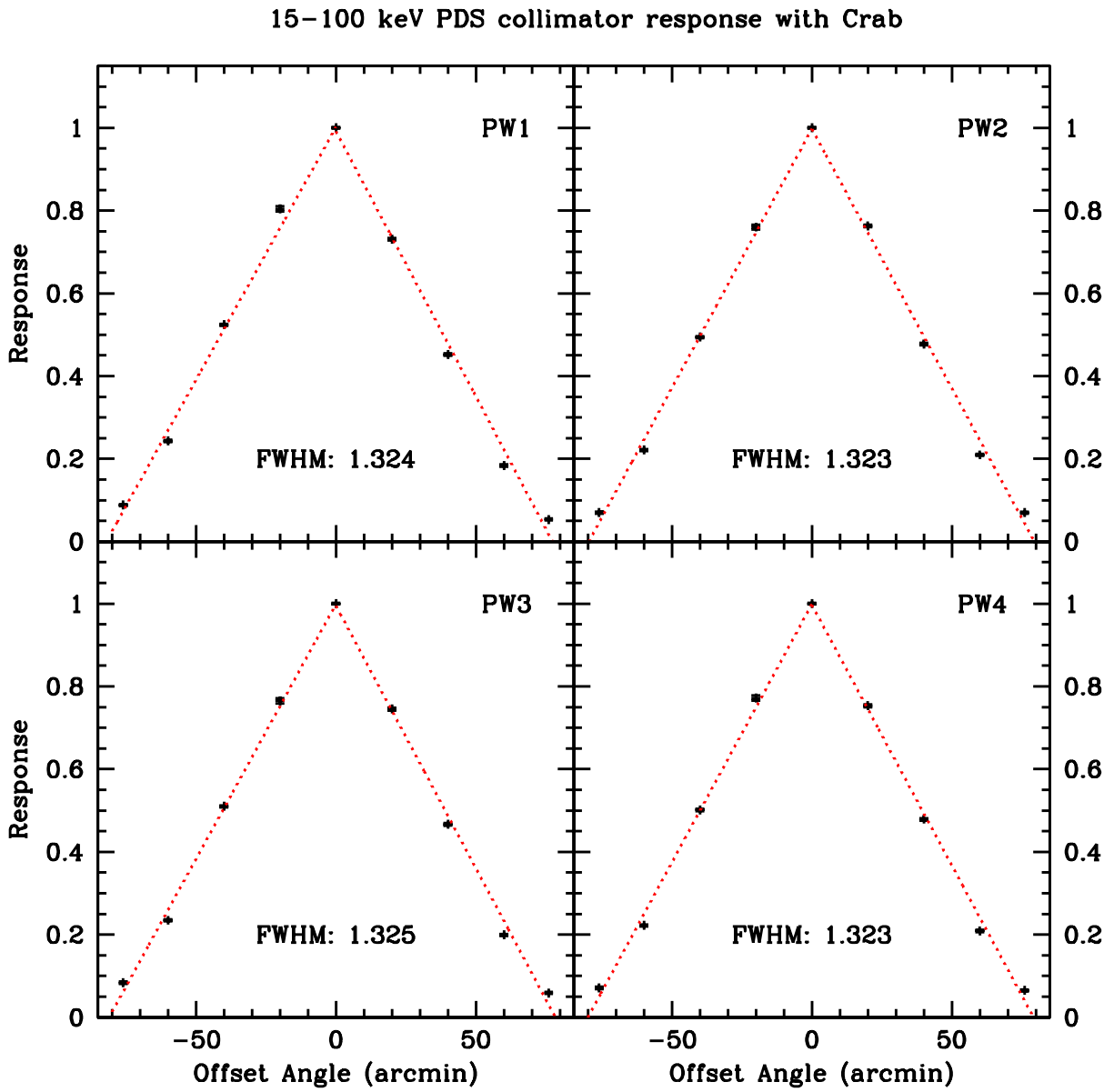


Figure 2: Angular response of the PDS collimators for each phoswich unit measured from offset observations of the Crab in 15–100 keV.

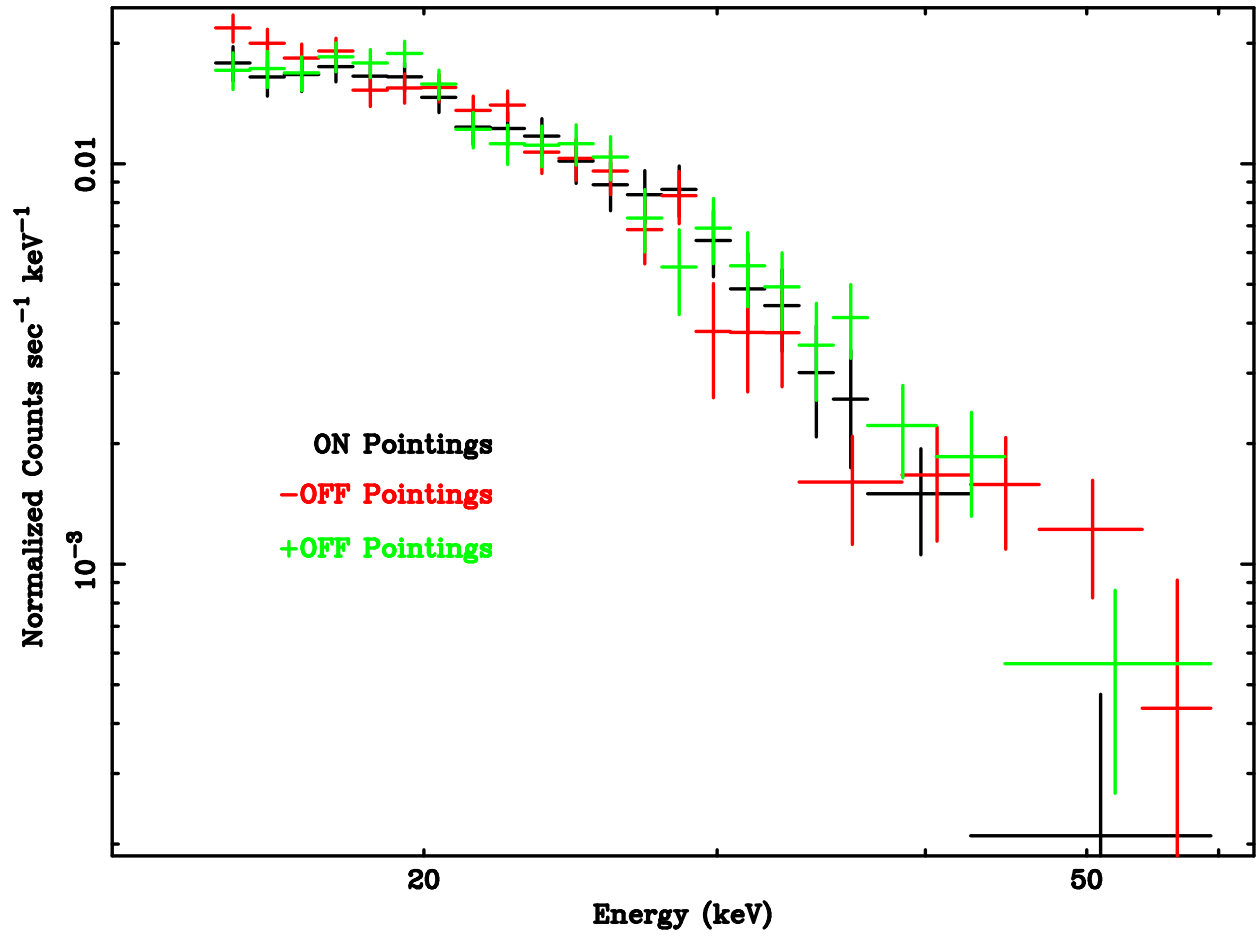


Figure 3: Difference spectra $D_{\text{ON}}(E)$, $D_{+\text{OFF}}(E)$ and $D_{-\text{OFF}}$ obtained from the ON-source and OFF-source pointings.

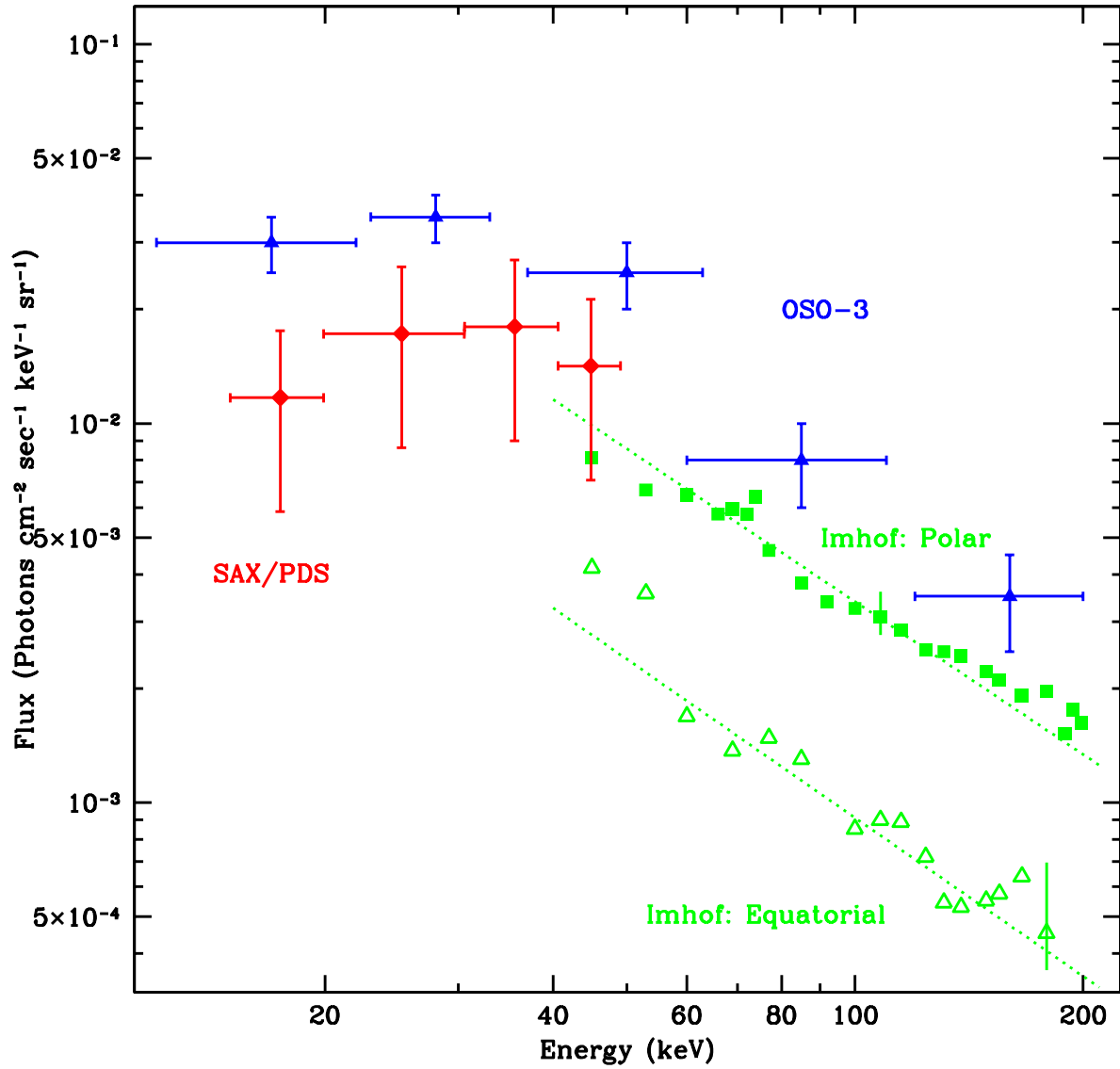


Figure 4: Comparison of the best fit albedo photon spectrum as derived by the PDS measurement (red points) with the results found by Schwartz and Peterson (*OSO-3* satellite²⁰, blue points) and by Imhof et al. (*1972-076B* satellite²¹, green points).

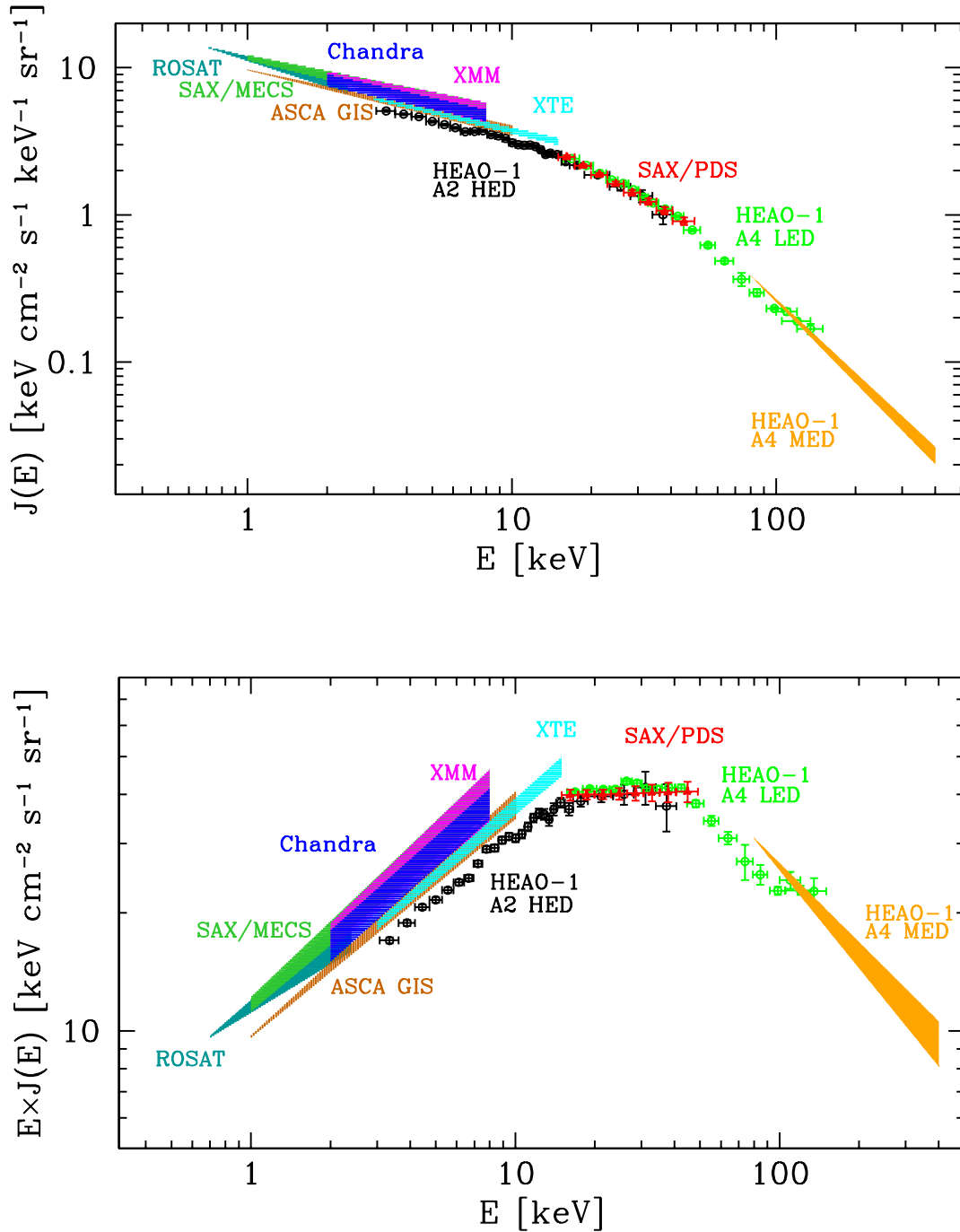


Figure 5: Total (unresolved plus resolved) CXB spectrum as observed with the PDS experiment (red points) assuming a PL model, compared with measurement results obtained with other missions. *Upper panel:* The energy spectrum $J(E)$. *Bottom panel:* The $E J(E)$ spectrum. The fitting parameters are listed in Table 1 of the main paper.

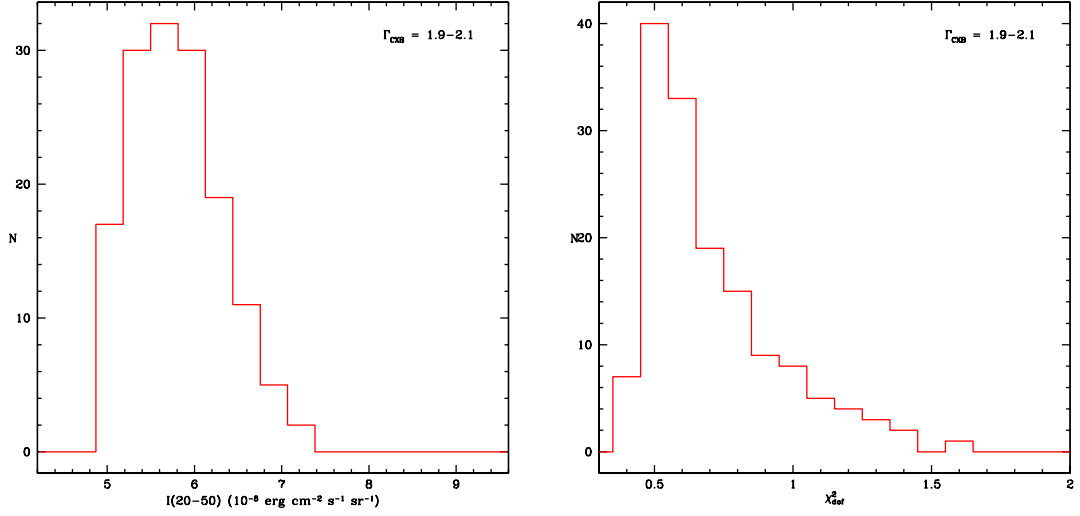


Figure 6: *Left panel:* Frequency distribution (146 trials) of the total CXB 20–50 keV integrated intensity in the case of a PL CXB model with Γ_{CXB} in the range 1.9–2.1. *Right panel:* Frequency distribution of the reduced χ^2 for the same data. See text.

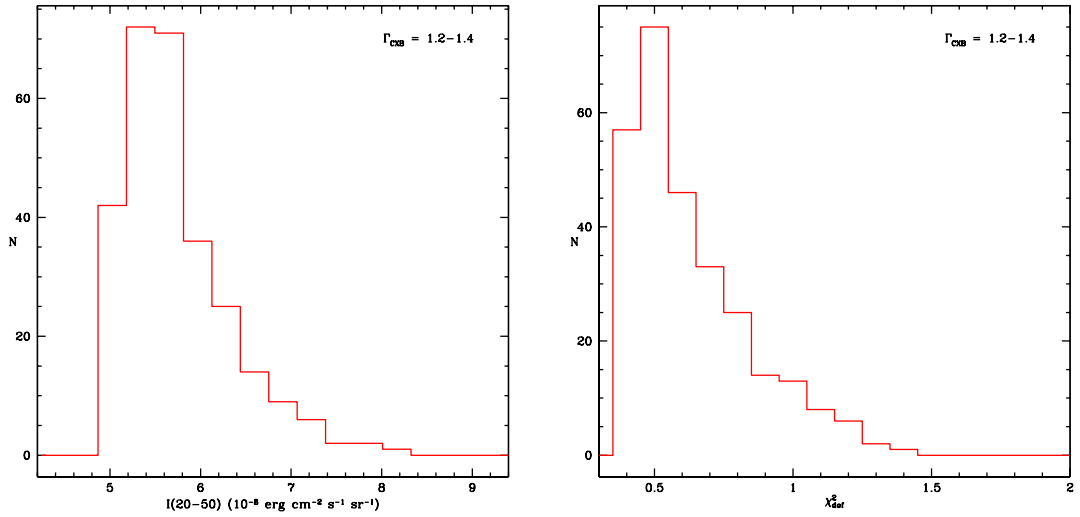


Figure 7: *Left panel:* Frequency distribution (280 trials) of the total CXB 20–50 keV integrated intensity in the case of a CUTOFFPL CXB model with Γ_{CXB} in the range 1.2–1.4. *Right panel:* Distribution of the reduced χ^2 for the same data. See text.

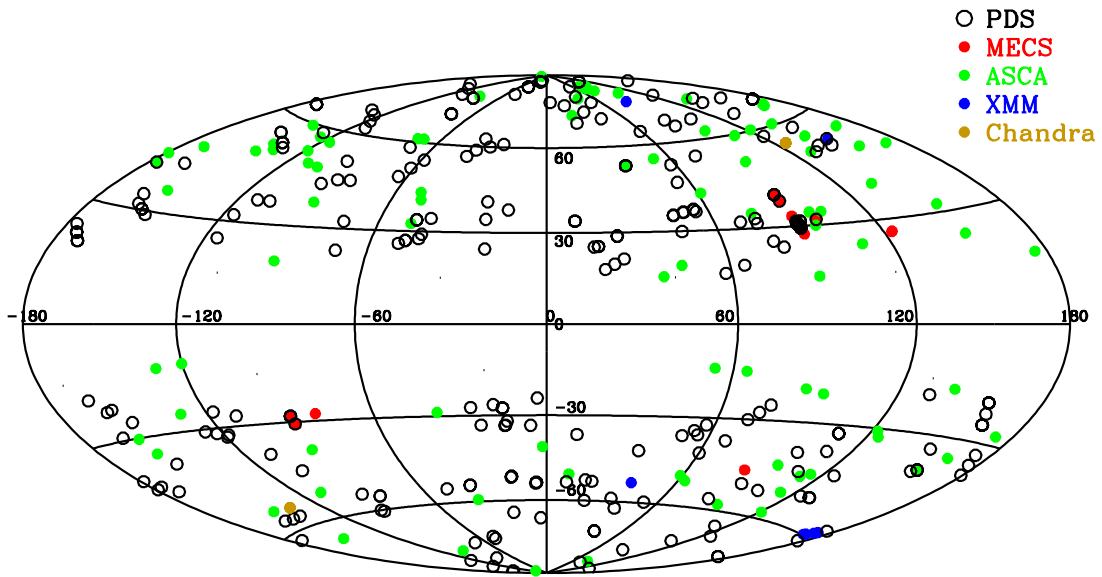


Figure 8: Sky covered by the PDS compared with that covered by different focusing missions for the unresolved CXB determination. The 172 PDS pointings correspond to 265 deg^2 . Sky coverage of focusing telescopes: 0.73 deg^2 (*MECS*²⁸); 50 deg^2 (*ASCA*²⁹); 1.2 deg^2 (*XMM-Newton*³⁰), 0.5 deg^2 (*Chandra*³¹). For the 34 *XMM-Newton* pointings used by De Luca & Molendi³², coverage is 5.5 deg^2 , but coordinates are not available.